

Cite this: *Dalton Trans.*, 2021, **50**,  
2616

# Highly efficient catalytic transfer hydrogenation of furfural over defect-rich amphoteric ZrO<sub>2</sub> with abundant surface acid–base sites†

Zekun Zhu,<sup>‡</sup> Lingling Yang,<sup>‡</sup> Changxuan Ke, Guoli Fan,<sup>‡</sup> \* Lan Yang<sup>‡</sup> and Feng Li<sup>‡</sup> \*

Currently, the catalytic transformation and utilization of biomass-derived compounds are of great importance to the alleviation of environmental problems and sustainable development. Among them, furfural alcohol derived from biomass resources has been found to be one of the most prospective biomass platforms for high-value chemicals and biofuels. Herein, high-surface-area ZrO<sub>2</sub> with abundant oxygen defects and surface acid–base sites was synthesized and used as a heterogeneous catalyst for the catalytic transfer hydrogenation of furfural into furfural alcohol using alcohol as a hydrogen donor. The as-synthesized ZrO<sub>2</sub> exhibited excellent catalytic performance with 98.2% FA conversion and 97.1% FOL selectivity, even comparable with that of a homogeneous Lewis acid catalyst. A series of characterization studies and experimental results revealed that acid sites on the surface of ZrO<sub>2</sub> could adsorb and activate the C=O bond in furfural and base sites could facilitate the formation of alkoxide species. The synergistic effect of surface acid–base sites affords a harmonious environment for the reaction, which is crucial for catalytic transfer hydrogenation of furfural with high efficiency. Furthermore, the as-prepared ZrO<sub>2</sub> catalyst also exhibited a potential application for the efficient catalytic transfer hydrogenation of a series of biomass-derived carbonyl compounds.

Received 7th January 2020,  
Accepted 19th January 2021

DOI: 10.1039/d0dt00055h

rsc.li/dalton

## 1. Introduction

Presently, diminishing fossil fuel reserves and deteriorating environmental problems have encouraged the development of economically efficient and environmentally friendly technologies for the preparation of renewable fuels and fine chemicals.<sup>1–5</sup> Furfural (FA), one of the most important renewable platform molecules, has been produced by the acid hydrolysis of five-carbon sugars contained in lignocellulosic biomass.<sup>6</sup> Due to the presence of the C=O bond in the branched chain and the C=C bond in the furan ring, FA can be selectively transformed to produce various valuable chemicals and biofuels (Fig. 1), such as furfural alcohol (FOL), tetrahydrofurfuryl alcohol (THFOL), furfurylamine, 2-methylfuran (2-MF), tetrahydrofuran (THF), cyclopentanone (CPO), 1,5-pentanediol (1,5-PDO), 1,4-butanediol (1,4-BDO), and so on.<sup>7–13</sup>

Among the above chemicals, FOL is one of the most interesting and valuable intermediates since it can be used for the production of thermostatic resins, synthetic fibers, foundry binders, farm chemicals, lubricants, lysine, vitamin C, *etc.*<sup>6,13</sup> Commercial preparation of FOL using FA as a raw material has been performed over various copper–chromite (Cu–Cr) catalysts either in the liquid phase or in the vapor phase for decades.<sup>14,15</sup> However, the main drawbacks of the copper–chromite catalyst are the moderate activity for FA hydrogenation and the toxic nature of chromium oxides, thereby causing high energy consumption and serious environmental pollution. To overcome the above problems, a variety of non-chromite based catalysts including precious metals (Pt, Pd, Ru, and Ir),<sup>16–18</sup> non-precious metals (Cu, Ni, and Fe),<sup>19–21</sup> and bimetallic alloys (Pt–M, Fe–M, Ni–M, and Cu–M) have been developed for the hydrogenation of FA to FOL.<sup>22–26</sup> However, poor selectivity of FOL originating from the unselective hydrogenation of the C=C bonds and cracking of the C–C bonds in FA, high cost of catalysts, and use of explosive molecular hydrogen under stringent reaction conditions are prominent barriers for large-scale applications.

During the past decade, for environmental, safety, and economic considerations, formic acid or non-corrosive alcohols have been used as hydrogen sources to replace explosive

State Key Laboratory of Chemical Resources Engineering, Beijing Advanced Innovation Center for Soft Matter Science and Engineering, Beijing University of Chemical Technology, Beijing, 100029, China. E-mail: fangl@mail.buct.edu.cn, lifeng@mail.buct.edu.cn; Fax: +861064425385; Tel: +861064451226

†Electronic supplementary information (ESI) available. See DOI: 10.1039/d0dt00055h

‡These authors contributed equally to this work.

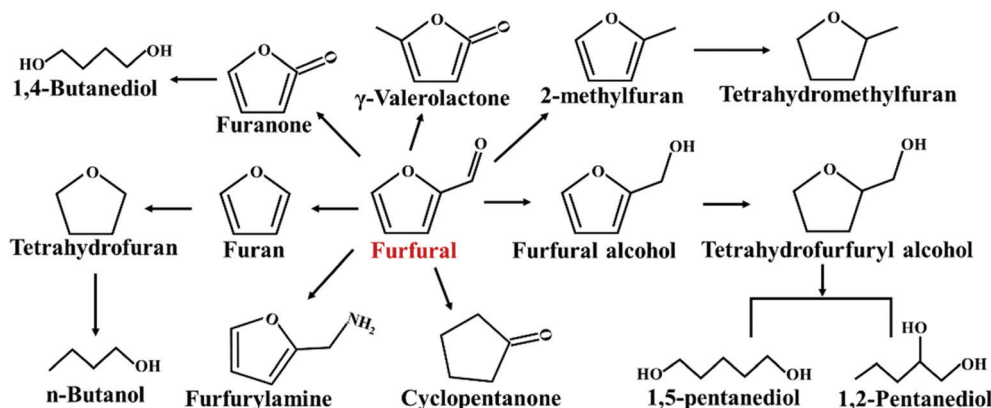


Fig. 1 Catalytic conversion of furfural to fuel components and chemicals.

molecular hydrogen for the catalytic transfer hydrogenation (CTH) of biomass to fine chemicals over several metal catalysts under mild conditions.<sup>27–30</sup> Meanwhile, carbonyl-selective hydrogenation of biomass, even in the presence of other active groups (alkoxyl groups, unsaturated carbon moieties, nitriles, *etc.*), has been achieved *via* the Meerwein–Ponndorf–Verley (MPV) reduction over several low-cost metal oxides. The performance of MPV catalysts is mainly affected by the Lewis acidity in the catalyst, which is responsible for the polarization of the carbonyl group in biomass materials.<sup>31–35</sup> To date, the CTH of FA to FOL over metal catalysts has been investigated and has achieved acceptable catalytic performance; furthermore, a few kinds of acid zeolites and basic metal oxides or hydroxides were also reported to be used as efficient catalysts for the CTH of FA to FOL.<sup>36–38</sup> For instance, Zhang *et al.* reported that a hydroxyapatite-encapsulated magnetic  $\gamma\text{-Fe}_2\text{O}_3$  ( $\gamma\text{-Fe}_2\text{O}_3\text{@HAP}$ ) catalyst yielded 95.3% selectivity to FOL at about 96.2% FA conversion.<sup>39</sup> They found that base sites play a positive role in the CTH of FA to FOL. Compared with the conventional hydrogenation of FA by  $\text{H}_2$ , CTH processes seem to be more economical, safer, and more eco-friendly, but they are still far from being satisfactory due to the low reaction activity toward hydrogen donors, high catalyst dosages, and low FOL selectivity. Hence, designing and developing environmentally friendly and high-performing heterogeneous catalysts is crucial for the CTH of FA to FOL from the perspective of the utilization of biomass resources and fuel economy.

Zirconium-based materials such as zirconium-beta zeolite, zirconium oxide or hydroxide, and Zr-doped metal oxides possess acidic and basic functionalities, as well as high thermal and chemical stability, which have been investigated as catalytic materials (*i.e.*, catalysts, supports, or promoters) for the transformation of biomass-derived molecules into valuable chemicals.<sup>40–43</sup> Steven V. Ley *et al.* prepared a partially hydrated  $\text{ZrO}_2$  catalyst from a zirconium hydroxide precursor, used it as a catalyst for the transfer hydrogenation of ketones and aldehydes *via* a mild and efficient flow procedure, and investigated the effect of flow conditions on catalytic performance systematically.<sup>42</sup> However, investigation on the synthesis and application of pure  $\text{ZrO}_2$  as a catalyst for

the CTH of biomass-derived molecules is limited so far, especially for the CTH of FA to FOL. From the perspective of catalytic applications, the catalytic performance of  $\text{ZrO}_2$  is closely associated with the specific surface area and the surface properties. However,  $\text{ZrO}_2$  obtained by conventional precipitation of zirconyl salts with ammonia or sodium hydroxide usually possesses a low surface area ( $70\text{--}150\text{ m}^2\text{ g}^{-1}$ ) and scarce surface acid–base sites after post-calcination treatment.<sup>44</sup> Hence, the practical application of the  $\text{ZrO}_2$  catalyst for the CTH of FA to FOL has been limited. Previously, we reported the successful synthesis of porous  $\text{ZrO}_2$  with large surface areas and controlled morphologies *via* a two-step solution-phase strategy.<sup>45</sup> The synthesized  $\text{ZrO}_2$  was used as a support for the fabrication of highly dispersed zirconium-based supported catalysts, which exhibited excellent catalytic performance for the hydrogenations of cinnamaldehyde and  $\gamma$ -valerolactone.<sup>46,47</sup>

In this work, we synthesized  $\text{ZrO}_2$  nanocrystals with large surface areas, porous structures, and abundant surface acid–base sites and oxygen defects by a two-step solution-phase strategy that we developed previously, and systematically investigated the influence of the surface acid–base sites of  $\text{ZrO}_2$  on the catalytic behavior of CTH of FA to FOL with alcohol as a mild hydrogen source. The results indicated that acid sites on the surface of  $\text{ZrO}_2$  are beneficial for the adsorption and activation of the  $\text{C}=\text{O}$  bond in FA, base sites are good for the formation of alkoxide species, and the synergistic effect of surface acid–base sites affords a harmonious environment for the CTH of FA, and thus the as-prepared  $\text{ZrO}_2$  catalyst exhibited excellent catalytic performance with a high 95.4% yield of FOL under mild conditions. To the best of our knowledge, there is no report about the application of such defect-rich amphoteric  $\text{ZrO}_2$  catalysts for the CTH of FA to produce FOL.

## 2. Experimental section

### 2.1 Materials

$\text{Zr}(\text{NO}_3)_4 \cdot 5\text{H}_2\text{O}$  (99.9%) and  $\text{NaBH}_4$  (99.7%) were purchased from Sigma-Aldrich, and FA (98.0%) and FOL (98.0%) were

purchased from J&K Scientific Ltd. 2-Propanol (2-PrOH) and other analytical grade reagents were purchased from Beijing Chemical Co. and used directly without further purification.

## 2.2 Preparation of catalysts

The ZrO<sub>2</sub> sample was prepared *via* a two-step solution-phase method.<sup>45</sup> Typically, two solutions were prepared prior to the synthesis. Zr(NO<sub>3</sub>)<sub>4</sub>·5H<sub>2</sub>O (0.01 mol) was ultrasonically dispersed in 40 mL of deionized water to form a clear salt solution A. NaBH<sub>4</sub> (0.15 mol) was dissolved in 40 mL of deionized water to form solution B. Solutions A and B were synchronously added to a colloid mill with the rotor rotating at a speed of 6000 rpm; a white slurry was formed after being mixed for 2 min, and the obtained slurry was sealed in a 100 mL autoclave and aged at 150 °C for 12 h. After cooling, the resulting precipitate was washed with deionized water and ethanol, dried at 70 °C for 12 h, and denoted as ZrO<sub>2</sub>. Furthermore, the as-prepared ZrO<sub>2</sub> was then calcined at 200, 400, and 600 °C for 8 h and marked as ZrO<sub>2</sub>-200, ZrO<sub>2</sub>-400, and ZrO<sub>2</sub>-600, respectively. For comparison, ZrO<sub>2</sub>-S was also prepared under similar experimental conditions using NaOH as a precipitant.

## 2.3 Characterization

Powder X-ray diffraction (XRD) data were recorded at room temperature on a Bruker D8 Advance system with a graphite-filtered Cu-K $\alpha$  radiation source ( $\lambda = 0.15418$  nm). The morphology and microstructure of the samples were observed using a Zeiss Supra 55 field-emission scanning electron microscope (FESEM) operating at an accelerating voltage of 20 kV and a JEOL 2100 high-resolution transmission electron microscope (HRTEM) operating at an accelerating voltage of 200 kV. Low-temperature N<sub>2</sub> adsorption-desorption measurements were performed using a Micromeritics ASAP 2020 instrument, and the surface area and pore size distribution were determined by using Brunauer-Emmett-Teller (BET) and nonlocal density functional theory (NL-DFT) models. X-ray photoelectron spectra (XPS) were collected using a Thermo VG ESCALAB250 X-ray photoelectron spectrometer with Al K $\alpha$  X-ray (1486.6 eV) as the excitation source. The oxygen storage capacity (OSC) of ZrO<sub>2</sub> samples was investigated by the oxygen pulse injection method. 100 mg of ZrO<sub>2</sub> sample was purged with He at 150 °C firstly, and the flow rate was set at 40 mL min<sup>-1</sup>. Then, the O<sub>2</sub>/He gas mixture (1:9, V/V) at a rate of 40 mL min<sup>-1</sup> was injected periodically into the sample until the signal area was constant. The number of surface oxygen vacancies ( $N_v$ ) was calculated based on the consumption of oxygen. *In situ* Fourier transform infrared (FT-IR) spectra of pyridine, furfural, and 2-PrOH adsorbed on catalysts were recorded on a Thermo Nicolet 380 spectrometer. 50 mg of ZrO<sub>2</sub> sample was pressed into a self-supporting wafer, which was placed in an evacuable IR cell with CaF<sub>2</sub> windows, evacuated at 200 °C for 2 h, and then cooled to room temperature. For pyridine adsorption, pyridine was introduced at room temperature after acquisition of the background spectrum; the sample was heated gradually to 200 °C under vacuum. For fur-

fural or 2-PrOH adsorption, the ZrO<sub>2</sub> sample was exposed to saturated vapour at room temperature firstly, and the physically adsorbed molecules were removed by evacuation. All the FT-IR spectra were recorded at 30 °C and normalized based on the sample weight. NH<sub>3</sub> temperature-programmed desorption (NH<sub>3</sub>-TPD) and CO<sub>2</sub> temperature-programmed desorption (CO<sub>2</sub>-TPD) were carried out on a Micromeritics Chemi-Sorb 2720 instrument. 100 mg ZrO<sub>2</sub> sample was loaded into a quartz tube and degassed by heating under He at 200 °C for 1 h to remove physically adsorbed species. NH<sub>3</sub> adsorption was performed at 100 °C in an NH<sub>3</sub>-He gas mixture (5:95, v/v) for 1.5 h; the residual NH<sub>3</sub> was removed by purging with He. Then the sample was heated to 700 °C at a heating rate of 10 °C min<sup>-1</sup>, and the desorbed NH<sub>3</sub> was monitored using a mass spectrometer. CO<sub>2</sub>-TPD was carried out by using a similar procedure. <sup>31</sup>P NMR spectra were acquired on a Bruker Avance III 400 WB solid-state spectrometer with a response frequency of 161.904 MHz using a 4 mm rotor at a spinning rate of 8 kHz. All samples were pre-treated under vacuum with the pressure below 10<sup>-3</sup> Pa for 10 h, and the preparation of TMPO adsorbed ZrO<sub>2</sub> samples was carried out according to the method reported by Zheng's group.<sup>48</sup> The chemical shift of <sup>31</sup>P resonance was referenced to adenosine triphosphate.

## 2.4 Catalytic test

The liquid phase catalytic transfer hydrogenation of FA was carried out in a 100 mL autoclave equipped with a timing heating system and a magnetic stirrer. Typically, 0.01 mol furfural, 0.2 g catalyst, and 0.1 mol 2-PrOH were added into the reactor, and air was purged out of the reactor with 2 MPa N<sub>2</sub> ten times. The reaction was initiated by stirring at a rate of 1000 rpm at a predefined temperature. After the reaction, the reactor was cooled in an ice-water bath and depressurized carefully. Qualitative and quantitative analyses of the obtained products were performed on an Agilent GC-7890B gas chromatograph equipped with a DB-WAX capillary column (30.0 m  $\times$  250  $\mu$ m  $\times$  0.25  $\mu$ m). The products were identified by comparison with known standards, and dodecane was used as an internal standard. In each case, the calculated carbon balance was above 96%. After the reaction, the catalyst was centrifuged, washed, dried at 70 °C overnight, and employed to investigate its reusability by adding a fresh substrate under similar reaction conditions.

# 3. Results and discussion

## 3.1 Structural analysis of catalysts

Fig. 2a shows the XRD pattern of the as-prepared ZrO<sub>2</sub> sample. All the intensive and broad diffraction peaks in the range of 10–80° can be well indexed to the tetragonal ZrO<sub>2</sub> (*t*-ZrO<sub>2</sub>) phase (JCPDS no. 42-1164), indicative of the highly pure and well-crystallized nature of the ZrO<sub>2</sub> sample. Fig. 2b shows the N<sub>2</sub> adsorption-desorption isotherms and pore size distribution of ZrO<sub>2</sub>. The isotherm is of complex type including types I and IV, indicating that the as-prepared ZrO<sub>2</sub> sample possesses

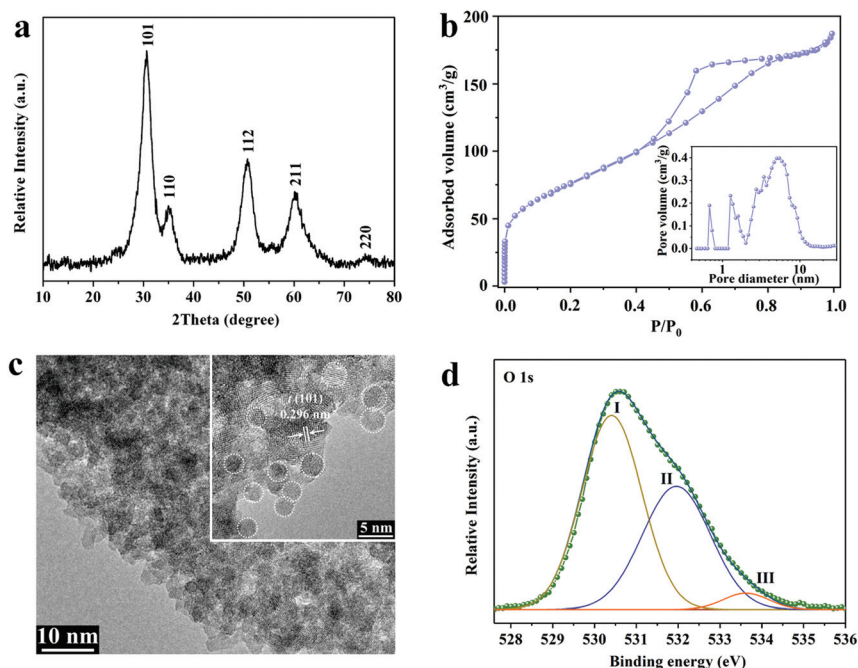


Fig. 2 XRD pattern (a), low-temperature nitrogen adsorption–desorption isotherm and pore size distribution (b), HRTEM image (c), and O 1s XPS spectra (d) of ZrO<sub>2</sub>.

microporous and mesoporous structure. The surface area is high up to 278 cm<sup>2</sup> g<sup>-1</sup>, and the total pore volume is about 0.289 cm<sup>3</sup> g<sup>-1</sup>. The pore size distribution reveals that ZrO<sub>2</sub> has abundant mesopores accompanied by a small amount of micropores. As presented in Table 1, the BET surface areas, the total pore volumes, and the average pore sizes of calcined ZrO<sub>2</sub> samples decrease slightly with the increase of the calcination temperature (Fig. S1†), demonstrating the good structural stability of the as-prepared ZrO<sub>2</sub>. The SEM image shows that ZrO<sub>2</sub> exhibits a compact configuration of homogeneous nanoparticles (Fig. S2†), which is quite different from those of ZrO<sub>2</sub>-S and commercial ZrO<sub>2</sub>-C samples (Fig. S3†). Elemental mappings in Fig. S2† indicate the homogeneous distributions of Zr and O species in ZrO<sub>2</sub> with a Zr/O atomic ratio of about

1 : 1.92, very close to the ideal stoichiometric value of the ZrO<sub>2</sub> phase. In line with the SEM result, the TEM image shows that the as-prepared ZrO<sub>2</sub> is composed of interconnected spherical particles of about 3 ± 2 nm in size (Fig. 2c), and sponge-like pores can be formed among the compactly arranged ZrO<sub>2</sub> nanoparticles. The clear lattice fringe with a *d*-spacing of 0.296 nm can be ascribed to the (101) plane of the *t*-ZrO<sub>2</sub> phase, further confirming the tetragonal phase of the as-prepared ZrO<sub>2</sub> sample.<sup>49</sup>

The surface/near-surface chemical states of Zr and O species on the ZrO<sub>2</sub> samples were investigated by XPS. The core levels of Zr 3d and O 1s can be identified, and no contaminant species corresponding to the boron element can be detected. In the fine Zr 3d spectrum (Fig. S4†), two peaks at

Table 1 The structural and textural data of the samples

| Sample                           | Crystal size <sup>a</sup> (nm) | S <sub>BET</sub> <sup>b</sup> (m <sup>2</sup> g <sup>-1</sup> ) | V <sub>total</sub> <sup>c</sup> (cm <sup>3</sup> g <sup>-1</sup> ) | V <sub>micro</sub> <sup>d</sup> (cm <sup>3</sup> g <sup>-1</sup> ) | S <sub>micro</sub> /S <sub>BET</sub> <sup>e</sup> | D <sup>f</sup> (nm) | O <sub>II</sub> /O <sub>I</sub> <sup>g</sup> | N <sub>v</sub> <sup>h</sup> (μmol g <sup>-1</sup> ) | Total acid sites <sup>i</sup> (mmol g <sup>-1</sup> ) | Total basic sites <sup>k</sup> (mmol g <sup>-1</sup> ) |
|----------------------------------|--------------------------------|---|--|--|---|---------------------|--|---|---|--|
| ZrO <sub>2</sub>                 | 3.5                            | 278   | 0.289  | 0.054  | 22.6  | 4.1                 | 0.70   | 238.5   | 0.524 (0.461) <sup>j</sup>                            | 1.702 (1.187) <sup>l</sup>                             |
| ZrO <sub>2</sub> -200            | 4.0                            | 245   | 0.261  | 0.036  | 18.1  | 4.2                 | 0.62   | 198.7   | 0.498 (0.356)   | 1.528 (1.104)  |
| ZrO <sub>2</sub> -400            | 4.6                            | 225   | 0.232  | 0.022  | 14.2  | 4.2                 | 0.59   | 168.4   | 0.211 (0.126)   | 0.722 (0.432)  |
| ZrO <sub>2</sub> -600            | 5.1                            | 173   | 0.222  | 0.008  | 6.5   | 5.4                 | 0.51   | 145.2   | 0.108 (0.078)   | 0.409 (0.298)  |
| ZrO <sub>2</sub> -S              | 19.5                           | 44  | 0.228  | —  | 0   | 16.8                | 0.42   | 118.7   | n.d.  | 0.312 (0.159)  |
| ZrO <sub>2</sub> -C              | 40.5                           | 12  | 0.022  | —  | 0   | 7.3                 | 0.24   | 38.2  | n.d.  | n.d.   |
| ZrO <sub>2</sub> -R <sup>m</sup> | 3.5                            | 258   | 0.272  | 0.048  | 19.5  | 4.1                 | 0.66   | 215.3   | 0.513 (0.425)   | 1.680 (1.098)  |

<sup>a</sup> Crystal size based on XRD and TEM results. <sup>b</sup> Specific surface area calculated by the BET method. <sup>c</sup> Single-point total pore volume calculated from nitrogen adsorption at *P*/*P*<sub>0</sub> = 0.994. <sup>d</sup> Micropore volume calculated by the NL-DFT method. <sup>e</sup> Micropore surface area calculated by the NL-DFT method. <sup>f</sup> Average pore diameter. <sup>g</sup> Determined by XPS of the O 1s region. <sup>h</sup> Determined by the oxygen pulse injection method. <sup>i</sup> The amount of total acid sites determined by NH<sub>3</sub>-TPD analysis. <sup>j</sup> The amount of medium and strong acid sites in the total amount of acid sites. <sup>k</sup> The amount of total base sites determined by CO<sub>2</sub>-TPD analysis. <sup>l</sup> The amount of medium and strong base sites determined by CO<sub>2</sub>-TPD analysis. <sup>m</sup> ZrO<sub>2</sub> catalyst reused 4 times.

about 181.8 and 184.1 eV can be assigned to Zr 3d<sub>5/2</sub> and Zr 3d<sub>3/2</sub>, respectively.<sup>50,51</sup> It is noteworthy that the binding energy of Zr 3d<sub>5/2</sub> is smaller than those of ZrO<sub>2</sub>-S and commercial ZrO<sub>2</sub>-C samples, reflecting the formation of more surface oxygen vacancies to some extent.<sup>43</sup> The O 1s fine spectrum was analyzed and is shown in Fig. 2d; the fitted peak at about 530.4 eV (referred to as I) is assigned to the lattice oxygen species in the structure of ZrO<sub>2</sub>, while two other peaks at around 531.7 eV (referred to as II) and 533.2 eV (referred to as III) correspond to both defect oxides or hydroxyl species in the subsurface and surface adsorbed CO<sub>2</sub>, respectively.<sup>52,53</sup> The amount of surface defects (*e.g.* oxygen vacancies) was estimated based on the O<sub>II</sub>/O<sub>I</sub> intensity ratio. As presented in Table 1, the O<sub>II</sub>/O<sub>I</sub> intensity ratio is much higher than those of contrastive ZrO<sub>2</sub> samples, mirroring the existence of abundant defects on the surface of ZrO<sub>2</sub>. Furthermore, quantitative analysis of the concentration of surface oxygen vacancies was determined by oxygen storage capacity (OSC) measurements. It is noted from Table 1 that the concentration of oxygen vacancies of the ZrO<sub>2</sub> sample is high up to 238.5 μmol g<sup>-1</sup>; meanwhile, the O<sub>II</sub>/O<sub>I</sub> ratio and the oxygen vacancies present a declining trend with the increase of the calcination temperature, which may result from the slightly increased particle size and improved crystallinity at high calcination temperatures.

As we know, surface acid–base sites play important roles in the catalytic behaviour of many heterogeneous catalysts. As for amphoteric ZrO<sub>2</sub>, surface acid–base sites are usually ascribed to the abundant surface Zr-OH species, unsaturated Zr<sup>4+</sup> cations, and oxygen vacancy. Fig. 3 shows the FT-IR spectra of different pyridine-adsorbed ZrO<sub>2</sub> samples. As for ZrO<sub>2</sub>, the absorption bands at 1457, 1491, and 1612 cm<sup>-1</sup> reveal the presence of Lewis acid (LA) sites, while the absorption bands at 1542 and 1638 cm<sup>-1</sup> demonstrate the presence of Brønsted acid (BA) sites.<sup>54–56</sup> We speculated that surface coordinatively unsaturated Zr<sup>4+</sup> cations and abundant surface defects are responsible for the generation of LA sites, and the presence of BA sites is related to the surface Zr-OH species. In addition,

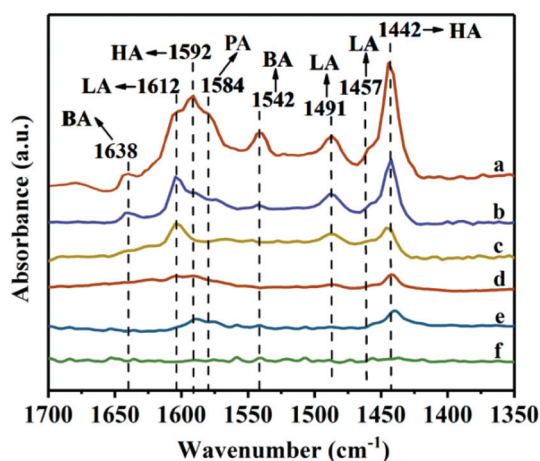


Fig. 3 FT-IR spectra of pyridine adsorbed onto ZrO<sub>2</sub> (a), ZrO<sub>2</sub>-200 (b), ZrO<sub>2</sub>-400 (c), ZrO<sub>2</sub>-600 (d), ZrO<sub>2</sub>-S (e), and ZrO<sub>2</sub>-C (f).

the absorption bands at 1442 and 1592 cm<sup>-1</sup> can be associated with H-bonding (HA) pyridine, and the absorption band at 1584 cm<sup>-1</sup> can be ascribed to the physically adsorbed (PA) pyridine.<sup>29</sup> Furthermore, the intensity of peaks corresponding to LA, BA, and HA decreases with the increase of the calcination temperature, reflecting a decreased amount of acid sites on ZrO<sub>2</sub> with the increase of the calcination temperature. In contrast, as for ZrO<sub>2</sub>-S, only weak peaks associated with LA and HA sites can be observed, and even no apparent peak is observed in the profile of the ZrO<sub>2</sub>-C sample. The Py-IR results reveal that the as-prepared ZrO<sub>2</sub> possesses more acid sites with a higher acid strength in comparison with those of ZrO<sub>2</sub>-S and ZrO<sub>2</sub>-C samples.

Solid-state <sup>31</sup>P NMR of adsorbed TMPO was also used to distinguish the Brønsted acid and Lewis acid on the as-prepared ZrO<sub>2</sub> samples.<sup>48,57,58</sup> As shown in Fig. 4, the <sup>31</sup>P spectrum of ZrO<sub>2</sub> can be fitted into four peaks with chemical shifts of 68, 62, 52, and 34 ppm, respectively. The peaks at about 68 ppm can be ascribed to the TMPO adsorbed on Brønsted acid sites, the two peaks at 62 and 52 ppm can be assigned to the TMPO adsorbed on two types of Lewis acid sites with different acid strengths (a larger chemical shift means a higher acid strength), and the peak at 34 ppm is attributed to physisorbed or mobile TMPO.<sup>48,57</sup> Notably, with increasing calcination temperature, the peak intensity at around 62 ppm decreases, while the peak intensity at around 52 ppm increases at first and then decreases. In addition, after calcination treatment, the Brønsted acid signal (chemical shift at 68 ppm) cannot be detected anymore, reflecting the decrease of the acid strength and the amount of acid sites over the calcined ZrO<sub>2</sub> samples. In contrast, ZrO<sub>2</sub>-S presents a weak peak at about 60 ppm, and only a weak peak corresponding to physisorbed TMPO can be observed for the ZrO<sub>2</sub>-C sample, indicating their poor acidic nature. The <sup>31</sup>P NMR results are well consistent with the FT-IR analysis.

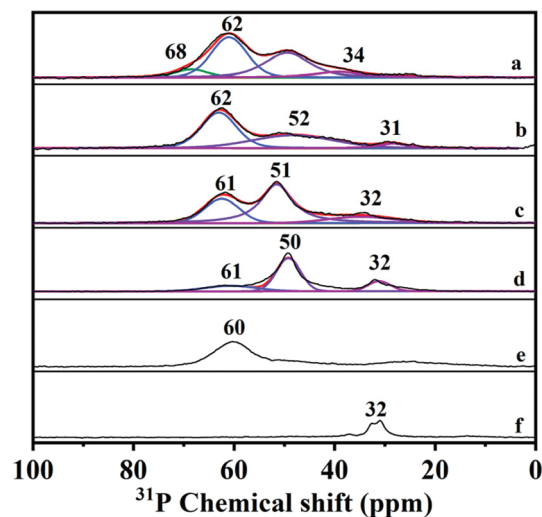


Fig. 4 <sup>31</sup>P MAS NMR spectra of TMPO adsorbed onto ZrO<sub>2</sub> (a), ZrO<sub>2</sub>-200 (b), ZrO<sub>2</sub>-400 (c), ZrO<sub>2</sub>-600 (d), ZrO<sub>2</sub>-S (e), and ZrO<sub>2</sub>-C (f).

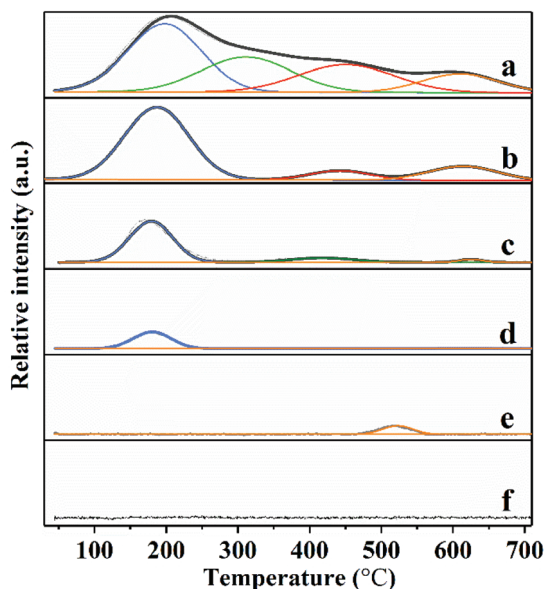


Fig. 5  $\text{NH}_3$ -TPD profiles of different  $\text{ZrO}_2$  samples:  $\text{ZrO}_2$  (a),  $\text{ZrO}_2$ -200 (b),  $\text{ZrO}_2$ -400 (c),  $\text{ZrO}_2$ -600 (d),  $\text{ZrO}_2$ -S (e), and  $\text{ZrO}_2$ -C (f).

Fig. 5 shows the  $\text{NH}_3$ -TPD of different  $\text{ZrO}_2$  samples. For the  $\text{ZrO}_2$  sample, the broad desorption peak of  $\text{NH}_3$  in the temperature region of 50–700 °C can be fitted into four peaks. The peaks at about 200, 320–450, and 600 °C are ascribed to the  $\text{NH}_3$  desorption from weak, medium, and strong acidic sites, respectively.<sup>43,59,60</sup> It should be noted that the acidity of  $\text{ZrO}_2$  is mostly medium strength, and the total acidic sites show a downward trend with increasing calcination temperature. In contrast, the  $\text{ZrO}_2$ -S sample shows only a weak desorption peak at around 520 °C, and no apparent desorption peak is observed for the commercial  $\text{ZrO}_2$ -C sample, indicating the scarce nature of acidic sites on the surface of  $\text{ZrO}_2$ -S and commercial  $\text{ZrO}_2$ -C samples. Furthermore, the relative proportions of different basic sites are obtained based on the integrated areas of these desorption peaks (Table 1), well consistent with those of Py-IR and  $^{31}\text{P}$  MAS NMR results.

Fig. 6 shows the  $\text{CO}_2$ -TPD of different  $\text{ZrO}_2$  samples. The  $\text{CO}_2$ -TPD profile of  $\text{ZrO}_2$  can be fitted into seven peaks. The peak centered at about 98 °C can be attributed to the physically adsorbed  $\text{CO}_2$ , whereas the peak centered at 150 °C can be associated with the  $\text{CO}_2$  desorption from weak basic sites (bicarbonate carbonate), three peaks centered at 260, 330, and 420 °C are ascribed to the  $\text{CO}_2$  desorption from medium-strength basic sites (bidentate carbonate), and two peaks at 490 and 560 °C are related to the  $\text{CO}_2$  desorption from strong basic sites (unidentate carbonate).<sup>41,61,62</sup> In contrast, the  $\text{CO}_2$  desorption peaks of  $\text{ZrO}_2$ -C and  $\text{ZrO}_2$ -S samples are not apparent, indicating that these two samples possess fewer basic sites than that of  $\text{ZrO}_2$ . Similarly, the basicity of  $\text{ZrO}_2$  is mostly medium strength, and the total basic sites decrease gradually with the increase of the calcination temperature (Table 1).

As we know, the adsorption behaviour of the reactants over the catalyst directly affects the extent of influence of the corres-

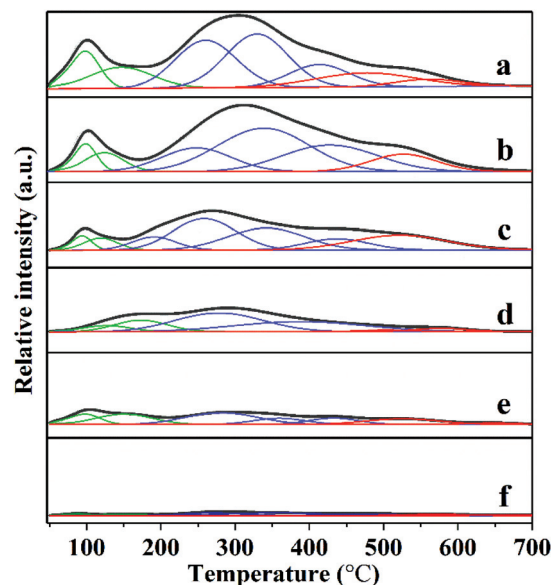


Fig. 6  $\text{CO}_2$ -TPD profiles of different  $\text{ZrO}_2$  samples:  $\text{ZrO}_2$  (a),  $\text{ZrO}_2$ -200 (b),  $\text{ZrO}_2$ -400 (c),  $\text{ZrO}_2$ -600 (d),  $\text{ZrO}_2$ -S (e), and  $\text{ZrO}_2$ -C (f).

ponding catalytic performance. In order to obtain more information on the surface-bonding state for reactants adsorbed on catalysts, *in situ* FT-IR studies of FA and isopropanol molecules adsorbed on typical  $\text{ZrO}_2$  samples were conducted, respectively. Fig. 7 shows the FT-IR spectra of FA-adsorbed  $\text{ZrO}_2$  samples. In all cases, the FT-IR spectra in the range of 1600–1750  $\text{cm}^{-1}$  present three absorption peaks at 1673, 1691, and 1721  $\text{cm}^{-1}$ , respectively. The adsorption peak at 1721  $\text{cm}^{-1}$  is ascribed to the *trans*-stretch vibration of the C=O bond in physisorbed FA based on the NIST database,<sup>63</sup> while the adsorption peaks at 1673 and 1691  $\text{cm}^{-1}$  should be assigned to the weak *cis*-stretch and *trans*-stretch vibrations of the C=O bond in FA due to the interaction of the carbonyl group with the surface Lewis acid sites.<sup>29,64</sup> Notably, the vibration intensity of the C=O band at 1673 and 1691  $\text{cm}^{-1}$

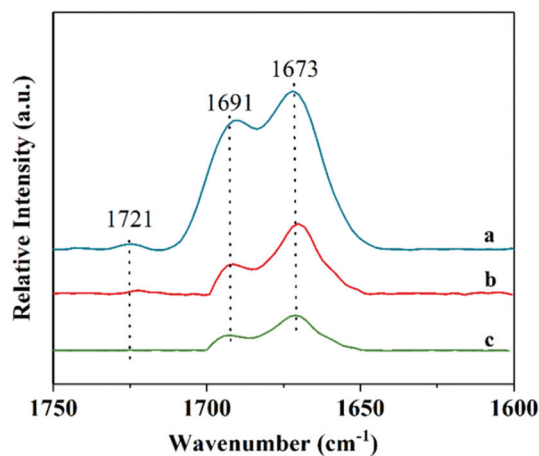


Fig. 7 FT-IR spectra of FA adsorbed onto  $\text{ZrO}_2$  (a),  $\text{ZrO}_2$ -S (b), and  $\text{ZrO}_2$ -C (c).

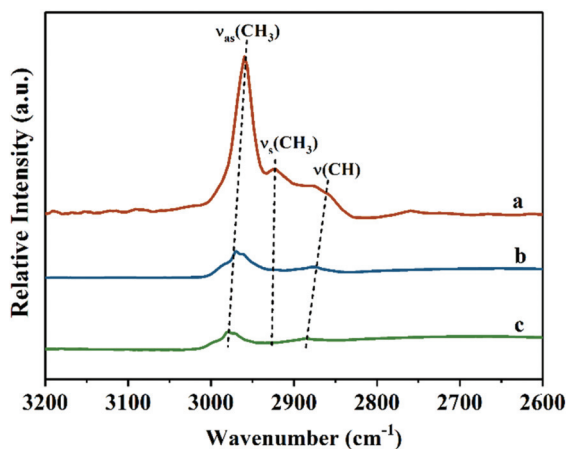


Fig. 8 FT-IR spectra of 2-PrOH adsorbed onto  $\text{ZrO}_2$  (a),  $\text{ZrO}_2\text{-S}$  (b), and  $\text{ZrO}_2\text{-C}$  (c).

increases in the order  $\text{ZrO}_2\text{-C} < \text{ZrO}_2\text{-S} < \text{ZrO}_2$ , reflecting that  $\text{ZrO}_2$  possesses superior adsorption capacity for FA to those of  $\text{ZrO}_2\text{-S}$  and  $\text{ZrO}_2\text{-C}$  samples. This phenomenon may originate from the existence of abundant surface defects on the as-prepared  $\text{ZrO}_2$ , which is beneficial for the chemisorption of FA.

FT-IR spectra of 2-PrOH-adsorbed samples were also measured and are shown in Fig. 8. Due to the interaction between the acidic CH groups in 2-PrOH and the basic sites of

the tested samples, three absorption peaks corresponding to the CH stretching modes ( $\nu(\text{CH})$ ,  $\nu_{\text{as}}(\text{CH}_3)$ ,  $\nu_{\text{s}}(\text{CH}_3)$ ) can be observed after 2-PrOH adsorption on the tested samples, and the vibration intensity of CH groups increases in the order  $\text{ZrO}_2\text{-C} < \text{ZrO}_2\text{-S} < \text{ZrO}_2$ , reflecting that the as-prepared  $\text{ZrO}_2$  possesses superior adsorption capacity for 2-PrOH to those of  $\text{ZrO}_2\text{-S}$  and  $\text{ZrO}_2\text{-C}$  samples. Furthermore, compared with those of contrastive  $\text{ZrO}_2$  samples, the  $\nu(\text{CH})$  and  $\nu_{\text{as}}(\text{CH}_3)$  bands in the spectrum of the as-prepared  $\text{ZrO}_2$  were red-shifted clearly, resulting from the interaction of basic sites in  $\text{ZrO}_2$  and the acidic methyl hydrogen atoms in 2-PrOH, which is beneficial for the deprotonation of 2-PrOH during the hydrogenation process.<sup>65</sup>

### 3.2 Catalytic performance of different $\text{ZrO}_2$ catalysts

All the above characterization results indicate that the as-prepared defect-rich  $\text{ZrO}_2$  with abundant surface acid-base sites may be a superior catalyst for the CTH of FA to FOL. The catalytic performance of the  $\text{ZrO}_2$  catalyst was first investigated using 2-PrOH as the hydrogen donor. As shown in Fig. 9a, the conversion of FA increases almost linearly from 57.8% to 91.6% with relatively high FOL selectivity (>98.1%) in the initial 3 h at 170 °C; ~0.68% difurfuryl ether (DFE) and ~1.02% 4-(2-furyl)-3-buten-2-one (FAT) are detected as the main by-products. The formation of DEF is caused by the intermolecular dehydration of the formed FOL, while the for-

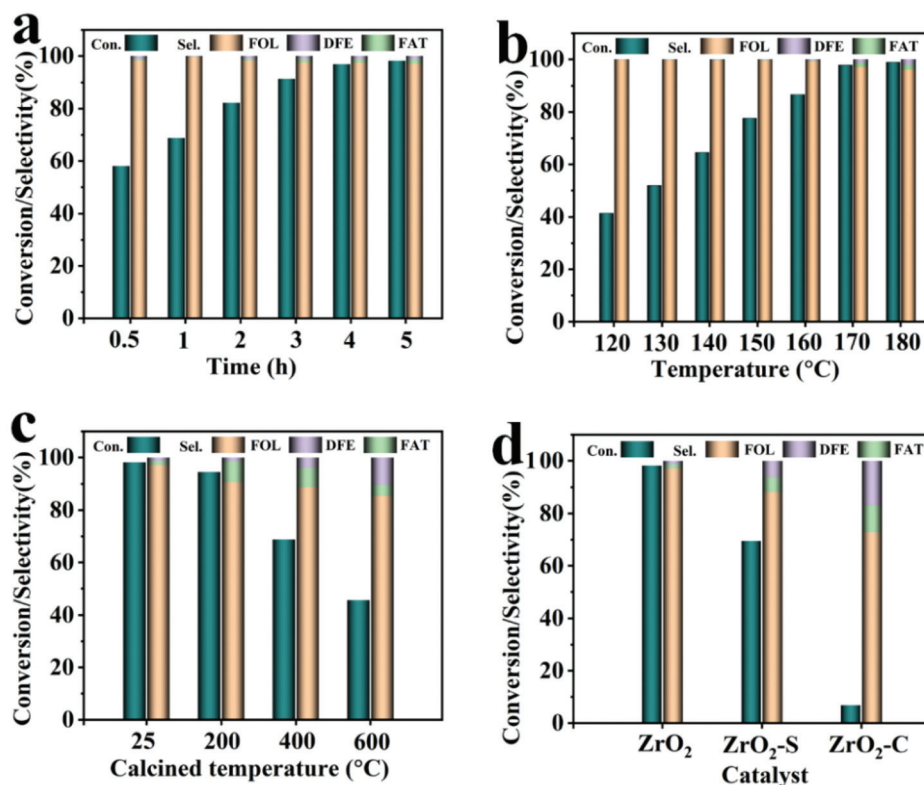


Fig. 9 Effects of the reaction time (a) and reaction temperature (b) on the CTH of FA over the  $\text{ZrO}_2$  catalyst. CTH of FA over  $\text{ZrO}_2$  calcinated at different temperatures (c) and with different  $\text{ZrO}_2$  contrastive samples (d). Reaction conditions: substrate, 0.01 mol; solvent, 0.1 mol; catalyst, 0.2 g; 2 MPa  $\text{N}_2$  atmosphere; stirring speed, 1000 rpm.

mation of FAT is caused by the intramolecular dehydration of 4-(2-furyl)-4-hydroxy-butan-2-one, which is generated from the condensation between FA and acetone.<sup>66–70</sup> The possible reaction pathways and the corresponding products over the as-prepared ZrO<sub>2</sub> catalyst are shown in Fig. S5.† As we further increase the reaction time to 5 h, the conversion of FA remains almost unchanged, but the selectivity towards FOL decreases to 97.1%. Notably, the conversion of FA increases from 41.2% to 98.2% as the reaction temperature increases from 120 °C to 170 °C, and the FOL selectivity remains above 97% (Fig. 9b). However, further increasing the reaction temperature to 180 °C is not only unfavourable for the conversion of FA but also causes a decline of FOL selectivity (96.1%) because of the formation of more DFE by-products (2.2%), reflecting that high temperature may be beneficial for the etherification of the newly formed FOL.<sup>66,67</sup>

The influence of different hydrogen donors on the CTH of FA to FOL over the as-prepared ZrO<sub>2</sub> catalyst was studied (Table 2). In contrast to using secondary alcohols (2-PrOH, 2-butanol) as hydrogen donors, lower FA conversion was obtained when using primary alcohols (1-propanol, 1-butanol) or cyclohexanol as hydrogen donors, which may result from the difficulty in deprotonation of primary alcohols and the strong steric effect of the cyclol structure.<sup>68</sup> Meanwhile, more side reactions such as self-condensation of the aldehyde formed after dehydrogenation of the hydrogen donor, as well as etherification of alcohol occurred when using a primary alcohol as the hydrogen donor, leading to an unsatisfactory FOL selectivity. Hence, the optimized reaction conditions (5 h, 170 °C, 2-PrOH as a hydrogen donor) were chosen and used in the comparison study.

The CTH of FA to FOL over ZrO<sub>2</sub> calcinated at different temperatures was investigated (Fig. 9c). With the increase of the calcination temperature, the FA conversion and FOL selectivity decreased significantly; meanwhile, the selectivity towards DFE increased from 1.5% to 3.9% and 10.3%, and the selectivity towards 4-(2-furyl)-3-buten-2-one (FAT) decreased from 7.8% to 7.3% and 4.2%, respectively. As we know, Lewis acid sites can interact with methyl hydrogen atoms in acetone molecules to form the electronegative intermediate, which can attack the electropositive C atom of C=O in FA and form the final FAT by-product.<sup>69,70</sup> The decreased selectivity towards FAT may be originated from the decrease of acid sites in the

calcined ZrO<sub>2</sub> samples. Furthermore, the catalytic performance of contrastive ZrO<sub>2</sub> catalysts was also investigated (Fig. 9d). The conversions of FA over ZrO<sub>2</sub>-S and commercial ZrO<sub>2</sub>-C catalysts under the optimized reaction conditions are 69.5% and 6.8%, and the selectivities towards FOL are 88.2% and 72.8%, respectively, which are much lower than those of the as-prepared ZrO<sub>2</sub> catalyst.

To deeply understand how surface acid sites and base sites affect the CTH of FA to FOL, H<sub>2</sub>SO<sub>4</sub> and N(CH<sub>2</sub>CH<sub>3</sub>)<sub>3</sub> were used as homogeneous catalysts under the optimized reaction conditions. As presented in Table 3, H<sub>2</sub>SO<sub>4</sub>, a typical Brønsted acid, gives 10.1% FA conversion, 37.7% FOL selectivity, and 62.3% DFE selectivity (entry 1), indicating that Brønsted acid can catalyse the CTH of FA to FOL. N(CH<sub>2</sub>CH<sub>3</sub>)<sub>3</sub>, a homogeneous base, affords poor catalytic performance (entry 2). However, when Sc(OTf)<sub>3</sub> was used as a homogeneous Lewis acid catalyst (entry 3), the FA conversion reaches up to 99.2%, and the selectivity towards FOL is 98.9%. Based on the above results, we deduced that both Lewis and Brønsted acid sites could act as active sites for the CTH of FA, the catalytic activity is mainly affected by Lewis acid sites, and the surface base sites play a promotional role in the CTH of FA.

Poisoning tests were performed to investigate the influence of acid sites on the CTH of FA over the ZrO<sub>2</sub> catalyst. 2,6-Dimethylpyridine (diPy) was added to block the surface Brønsted acid sites, while pyridine (Py) was used as a blocker for both surface Lewis and Brønsted acid sites.<sup>56</sup> As presented in Table 3, the conversion of FA decreases to 84.8% with almost unchanged FOL selectivity after the surface Brønsted acid sites of ZrO<sub>2</sub> were poisoned by diPy (entry 5). However, after being poisoned by Py, the FA conversion over Py poisoned ZrO<sub>2</sub> (ZrO<sub>2</sub>-py) further decreases to 66.9% with slightly decreasing FOL selectivity. Meanwhile, the selectivity towards DFE is on the rise, while the selectivity towards FAT shows a downward trend (entry 6). The slightly enhanced selectivity towards DEF is probably caused by the inhibition of aldol condensation between FA and acetone.

The reusability of the as-prepared ZrO<sub>2</sub> catalyst was studied representatively. It is noteworthy that the reused catalyst ZrO<sub>2</sub>-R exhibits a slightly decreased catalytic performance (95.3% FA conversion and 96.2% FOL selectivity) in the fourth cycle

**Table 2** CTH of FA using different hydrogen donors<sup>a</sup>

| Hydrogen donor | Con. (%) | Sel. (%) |
|----------------|----------|----------|
| 1-Propanol     | 60.4     | 84.2     |
| Cyclohexanol   | 80.2     | 54.5     |
| 1-Butanol      | 62.4     | 61.8     |
| 2-Butanol      | 89.5     | 83.8     |
| 2-PrOH         | 98.2     | 97.1     |

<sup>a</sup> Reaction conditions: Substrate, 0.01 mol; solvent, 0.1 mol; catalyst, 0.2 g; reaction temperature, 170 °C; reaction time, 5 h; 2 MPa N<sub>2</sub> atmosphere; stirring speed, 1000 rpm.

**Table 3** Transformation of FA to FOL over various catalysts<sup>a</sup>

| Entry          | Catalysts  | Con. (%) | Sel. (%) |      |     |
|----------------|--|----------|----------|------|-----|
|                |  |          | FOL      | DFE  | FAT |
| 1 <sup>b</sup> | H <sub>2</sub> SO <sub>4</sub>                   | 10.1     | 37.7     | 62.3 | 0   |
| 2 <sup>c</sup> | N(CH <sub>2</sub> CH <sub>3</sub> ) <sub>3</sub> | 6.6      | 86.1     | —    | —   |
| 3              | Sc(OTf) <sub>3</sub>                             | 99.2     | 98.9     | 0.4  | 0.7 |
| 4              | ZrO <sub>2</sub>                                 | 98.2     | 97.1     | 1.8  | 1.1 |
| 5              | ZrO <sub>2</sub> -dipy                           | 84.8     | 97.3     | 1.5  | 1.2 |
| 6              | ZrO <sub>2</sub> -py                             | 66.9     | 95.6     | 2.9  | 1.1 |

<sup>a</sup> Reaction conditions: Furfural, 0.01 mol; 2-PrOH, 0.1 mol; catalyst, 0.2 g; reaction temperature, 170 °C; reaction time, 5 h; 2 MPa N<sub>2</sub> atmosphere; stirring speed, 1200 rpm. <sup>b</sup> Catalyst amount, 5 μmol. <sup>c</sup> Catalyst amount, 10 μmol.

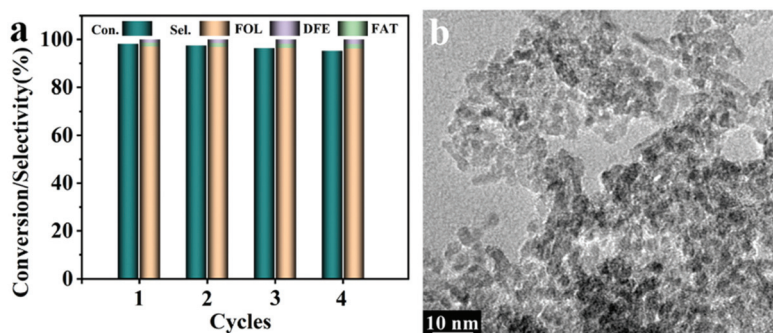


Fig. 10 Recyclability of  $\text{ZrO}_2$  in the CTH of FA (a). TEM image (b) of  $\text{ZrO}_2$  reused after four consecutive runs.

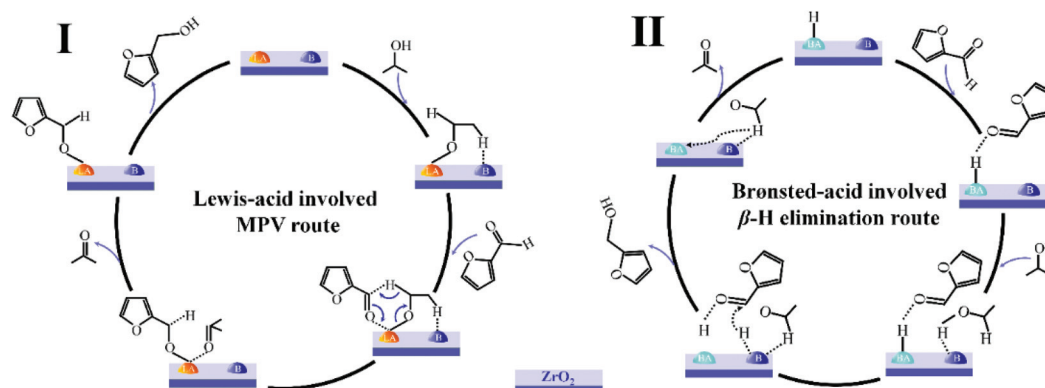
(Fig. 10a). Systematic characterization studies of the reused catalyst were carried out, and the relevant results are presented in Table 1. Compared with the fresh  $\text{ZrO}_2$  catalyst, the structure, surface area, and particle size of the reused catalyst remain almost unchanged (Table 1 and Fig. 10b). The XPS result shows that the ratio of surface  $\text{O}_{\text{II}}$  to  $\text{O}_{\text{I}}$  species decreases slightly from 0.70 to 0.66, and the total surface acid sites and base sites show a slight decrease, which probably might be the reason for the decreased catalytic performance over the reused  $\text{ZrO}_2$ -R catalyst.

### 3.3 Reaction mechanism for the CHT of FA

The above-mentioned facts revealed that the excellent catalytic performance over the as-prepared  $\text{ZrO}_2$  is not only affected by the surface acid properties but is also influenced by the synergistic effect of acid and base sites. Based on our experimental results, the CTH of FA to FOL with 2-PrOH over the as-prepared  $\text{ZrO}_2$  may proceed through two reaction routes: one follows the MPV reduction pathway related to surface Lewis acid sites, and the other follows a pathway related to surface Brønsted acid sites (Scheme 1). For the MPV reaction route, base sites can adsorb 2-PrOH and assist the formation of isopropoxide, and FA was also adsorbed on Lewis acid sites simultaneously. Then, transfer of hydrogen, a coordinated process, proceeds *via* a six-membered ring transition state formed between 2-PrOH and

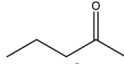
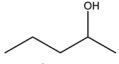
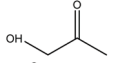
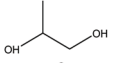
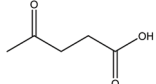
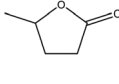
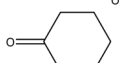
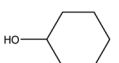
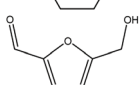
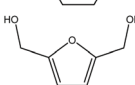
FA. Subsequently, the hydride ion transferred from the surface-adsorbed isopropoxide attacks the aldehyde group of FA to yield FOL, and 2-PrOH is converted to acetone consequently (Scheme 1(I)). In the case of the  $\alpha$ -H elimination route, the proton from Brønsted acid sites can interact with FA *via* coordinating with the O atom in the aldehyde group to weaken the C=O bond, resulting in the formation of protonated FA. Meanwhile, base sites can adsorb 2-PrOH and abstract a hydrogen atom from the alcoholic group to form isopropoxide. Subsequently, the  $\alpha$ -H atom is removed to form the corresponding acetone, and the generated active hydrogen attacks the protonated FA to generate FOL (Scheme 1(II)). In both cases, the synergistic effect of surface acid–base sites affords a harmonious environment for the hydrogenation of FA to FOL.

The CTH of a series of biomass-derived compounds containing carbonyl groups was also investigated to verify the applicability and feasibility of the  $\text{ZrO}_2$  catalyst. As shown in Table 4, in all cases, conversions above 90% are achieved over the  $\text{ZrO}_2$  catalyst, and the selectivities towards the target products are more than 85%. The results further indicate that the defect-rich  $\text{ZrO}_2$  with abundant surface acid–base sites can work as an ideal catalyst for the CTH of carbonyl compounds, reflecting its potential applications in the efficient exploitation and utilization of biomass-derived compounds.



Scheme 1 Proposed Lewis acid (I) and Brønsted acid (II) involved reaction mechanisms for the CTH of FA with 2-PrOH over the  $\text{ZrO}_2$  catalyst.

**Table 4** Catalytic transfer hydrogenation of different carbonyl compounds over the as-prepared ZrO<sub>2</sub> catalyst<sup>a</sup>

| Entry | Substrates  | Products  | Con. (%) | Sel. (%) |
|-------|---|---|----------|----------|
| 1     |  |  | 98.6     | 96.1     |
| 2     |  |  | 99.2     | 98.1     |
| 3     |  |  | 92.1     | 87.4     |
| 4     |  |  | 87.9     | 98.3     |
| 5     |  |  | 95.3     | 97.5     |

<sup>a</sup> Reaction conditions: Substrate, 0.01 mol; 2-PrOH, 0.1 mol; catalyst, 0.2 g; reaction temperature, 170 °C; reaction time, 8 h; 2 MPa N<sub>2</sub> atmosphere; stirring speed, 1000 rpm.

## 4. Conclusions

In this work, defect-rich ZrO<sub>2</sub> with abundant surface acid–base sites was prepared *via* a two-step solution-phase strategy and employed as a heterogeneous acid–base catalyst for the catalytic transfer hydrogenation of FA to FOL using alcohol as a hydrogen donor. The as-prepared ZrO<sub>2</sub> catalyst exhibited excellent catalytic performance with 98.2% FA conversion and 97.1% FOL selectivity in 5 h at 170 °C under a nitrogen atmosphere, even comparable to that of a homogeneous Lewis acid catalyst. A series of characterization studies and experiments revealed that abundant surface acid–base sites are of crucial importance for the efficient CTH of FA; acid sites on ZrO<sub>2</sub> can adsorb FA and activate the C=O bond in FA, while base sites are good for the formation of alkoxide species. The synergistic effect of surface acid–base sites affords a harmonious environment for the hydrogenation reaction. The as-formed defect-rich ZrO<sub>2</sub> catalyst was also efficient for the hydrogenation of a series of carbonyl compounds. Such a highly efficient and cost-effective amphoteric acid–base ZrO<sub>2</sub> catalyst provides potential applications for the efficient transformation and utilization of biomass resources, which is of great significance in terms of sustainable economic and ecological development.

## Conflicts of interest

There are no conflicts to declare.

## Acknowledgements

We greatly acknowledge the financial support from the National Natural Science Foundation of China (21991102, 21776017, 21521005, 21627813), the Joint Funds of the National Natural Science Foundation of China (U19B6002) and the Fundamental Research Funds for the Central Universities (XK1802-6).

## Notes and references

- Z. R. Zhang, J. L. Song and B. X. Han, *Chem. Rev.*, 2017, **117**, 6834–6880.
- D. L. Sun, S. Sato, W. Ueda, A. Primo, H. Garcia and A. Corma, *Green Chem.*, 2016, **18**, 2579–2597.
- T. Ennaert, J. V. Aelst, J. Dijkmans, R. D. Clercq, W. Schutyser, M. Dusselier, D. Verboekend and B. F. Sels, *Chem. Soc. Rev.*, 2016, **45**, 584–611.
- M. Besson, P. Gallezot and C. Pinel, *Chem. Rev.*, 2014, **114**, 1827–1870.
- F. J. Liu, L. Wang, Q. Sun, L. F. Zhu, X. J. Meng and F. S. Xiao, *J. Am. Chem. Soc.*, 2012, **134**, 16948–16950.
- X. D. Li, P. Jia and T. F. Wang, *ACS Catal.*, 2016, **6**, 7621–7640.
- M. J. Taylor, L. Jiang, J. Reichert, A. C. Papageorgiou, S. K. Beaumont, K. Wilson, A. F. Lee, J. V. Barth and G. Kyriakou, *J. Phys. Chem. C*, 2017, **121**, 8490–8497.
- C. Li, G. Y. Xu, X. H. Liu, Y. Fu and Y. Zhang, *Ind. Eng. Chem. Res.*, 2017, **56**, 8843–8849.
- M. Chatterjee, T. Ishizaka and H. Kawanami, *Green Chem.*, 2016, **18**, 487–496.
- S. H. Zhu, Y. F. Xue, J. Guo, Y. L. Cen, J. G. Wang and W. B. Fan, *ACS Catal.*, 2016, **6**, 2035–2042.
- Y. L. Yang, Z. T. Du, Y. Z. Huang, F. Lu, F. Wang, J. Gao and J. Xu, *Green Chem.*, 2013, **15**, 1932–1940.
- F. B. Li, T. Lu, B. F. Chen, Z. J. Huang and G. Q. Yuan, *Appl. Catal., A*, 2014, **478**, 252–258.
- O. F. Aldosari, *J. Saudi Chem. Soc.*, 2019, **23**, 938–946.
- W. B. Gong, C. Chen, Y. Zhang, H. J. Zhou, H. M. Wang, H. M. Zhang, Y. X. Zhang, G. Z. Wang and H. J. Zhao, *ACS Sustainable Chem. Eng.*, 2017, **5**, 2172–2180.
- C. P. Jiménez-Gómez, J. A. Cecilia, D. Durán-Martín, R. Moreno-Tost, J. Santamaría-González, J. Mérida-Robles, R. Mariscal and P. Maireles-Torres, *J. Catal.*, 2016, **336**, 107–115.
- S. Bhogeswararao and D. Srinivas, *J. Catal.*, 2015, **327**, 65–77.
- P. Panagiotopoulou and D. G. Vlachos, *Appl. Catal., A*, 2014, **480**, 17–24.
- Y. Nakagawa, K. Takada, M. Tamura and K. Tomishige, *ACS Catal.*, 2014, **4**, 2718–2726.
- M. Manikandan, A. K. Venugopal, A. S. Nagpure, S. Chilukuri and T. Raja, *RSC Adv.*, 2016, **6**, 3888–3898.
- J. Zhang and J. Z. Chen, *ACS Sustainable Chem. Eng.*, 2017, **5**, 5982–5993.
- M. Manikandan, A. K. Venugopal, K. Prabu and R. K. Jha, *J. Mol. Catal. A: Chem.*, 2016, **417**, 153–162.
- M. Sankar, N. Dimitratos, P. J. Miedziak, P. P. Wells, C. J. Kiely and G. J. Hutchings, *Chem. Soc. Rev.*, 2012, **41**, 8099–8139.
- S. T. Thompson and H. H. Lamb, *ACS Catal.*, 2016, **6**, 7438–7447.
- K. Fulajtárova, T. Soták, M. Hronec, I. Vávra, E. Dobročka and M. Omastová, *Appl. Catal., A*, 2015, **502**, 78–85.

- 25 N. Pino, S. Sitthisa, Q. H. Tan, T. Souza, D. López and D. E. Resasco, *J. Catal.*, 2017, **350**, 30–40.
- 26 S. De, J. G. Zhang, R. Luque and N. Yan, *Energy Environ. Sci.*, 2016, **9**, 3314–3347.
- 27 M. Villaverde, T. F. Garetto and A. J. Marchi, *Catal. Commun.*, 2015, **58**, 6–10.
- 28 F. J. Liu, W. P. Kong, L. Wang, X. F. Yi, I. Noshadi, A. M. Zheng and C. Z. Qi, *Green Chem.*, 2015, **17**, 480–489.
- 29 Z. Gao, L. Yang, G. L. Fan and F. Li, *ChemCatChem*, 2016, **8**, 3769–3779.
- 30 Q. Wu, F. J. Liu, X. F. Yi, Y. C. Zou and L. L. Jiang, *Green Chem.*, 2018, **20**, 1020–1030.
- 31 W. L. Li, S. Z. Liu, H. Y. Wang, B. Gao, C. Y. Tu and Y. B. Luo, *Catal. Commun.*, 2020, **133**, 105845.
- 32 R. Cohen, C. R. Graves, S. T. Nguyen, J. M. L. Martin and M. A. Ratner, *J. Am. Chem. Soc.*, 2004, **126**, 14796–14803.
- 33 L. Bui, H. Luo, W. R. Gunther and Y. Román-Leshkov, *Angew. Chem., Int. Ed.*, 2013, **52**, 8022–8025.
- 34 R. S. Assary, L. A. Curtiss and J. A. Dumesic, *ACS Catal.*, 2013, **3**, 2694–2704.
- 35 J. L. Song, L. Q. Wu, B. W. Zhou, H. C. Zhou, H. L. Fan, Y. Y. Yang, Q. L. Meng and B. X. Han, *Green Chem.*, 2015, **17**, 1626–1632.
- 36 H. Li, S. Yang, A. Riisager, A. Pandey, R. S. Sangwan, S. Saravanamurugan and R. Luque, *Green Chem.*, 2016, **18**, 5701–5735.
- 37 C. T. Wang, Z. Q. Liu, L. Wang, X. Dong, J. Zhang, G. X. Wang, S. C. Han, X. J. Meng, A. M. Zheng and F. S. Xiao, *ACS Catal.*, 2018, **8**, 474–481.
- 38 M. Koehle and R. F. Lobo, *Catal. Sci. Technol.*, 2016, **6**, 3018–3026.
- 39 F. Wang and Z. H. Zhang, *ACS Sustainable Chem. Eng.*, 2017, **5**, 942–947.
- 40 E. Hernández-Ramírez, J. A. Wang, L. F. Chen, M. A. Valenzuela and A. K. Dalai, *Appl. Surf. Sci.*, 2017, **399**, 77–85.
- 41 X. Tang, L. Hu, Y. Sun, G. Zhao, W. W. Hao and L. Lin, *RSC Adv.*, 2013, **3**, 10277–10284.
- 42 C. Battilocchio, J. M. Hawkins and S. V. Ley, *Org. Lett.*, 2013, **15**, 2278–2281.
- 43 J. Wang, S. Jaenicke and G. K. Chuah, *RSC Adv.*, 2014, **4**, 13481–13489.
- 44 V. G. Deshmane and Y. G. Adewuyi, *Microporous Mesoporous Mater.*, 2012, **148**, 88–100.
- 45 W. P. Cao, J. Kang, G. L. Fan, L. Yang and F. Li, *Ind. Eng. Chem. Res.*, 2015, **54**, 12795–12804.
- 46 S. P. Wei, Y. T. Zhao, G. L. Fan, L. Yang and F. Li, *Chem. Eng. J.*, 2017, **322**, 234–245.
- 47 S. S. Liu, G. L. Fan, L. Yang and F. Li, *Appl. Catal., A*, 2017, **543**, 180–188.
- 48 A. M. Zheng, S. J. Huang, S. B. Liu and F. Deng, *Phys. Chem. Chem. Phys.*, 2011, **13**, 14889–14901.
- 49 D. Ávila-Brandé, R. Perezzan, E. Urones-Garrote and L. C. Otero-Díaz, *Inorg. Chem.*, 2011, **50**, 4640–4646.
- 50 M. K. Dongare, A. M. Dongare, V. B. Tare and E. Kemnitz, *Solid State Ionics*, 2002, **152–153**, 455–462.
- 51 S. Ram and A. Mondal, *Appl. Surf. Sci.*, 2004, **221**, 237–247.
- 52 Z. Y. Wang, Y. Lu, S. Yuan, L. Y. Shi, Y. Zhao, M. H. Zhang and W. Deng, *J. Colloid Interface Sci.*, 2013, **396**, 9–15.
- 53 M. A. Rahman, S. Rout, J. P. Thomas, D. McGillivray and K. T. Leung, *J. Am. Chem. Soc.*, 2016, **138**, 11896–11906.
- 54 Z. M. Ma, X. Meng, C. Yang, N. W. Liu, Y. T. Zhang and L. Shi, *Ind. Eng. Chem. Res.*, 2017, **56**, 5598–5606.
- 55 Y. Matsunaga, H. Yamazaki, T. Yokoi, T. Tatsumi and J. N. Kondo, *J. Phys. Chem. C*, 2013, **117**, 14043–14050.
- 56 W. Li, Y. Z. Li, G. L. Fan, L. Yang and F. Li, *ACS Sustainable Chem. Eng.*, 2017, **5**, 2282–2291.
- 57 K. Shimizu, T. N. Venkatraman and W. G. Song, *Appl. Catal., A*, 2002, **224**, 77–87.
- 58 H. G. Yu, H. J. Fang, H. L. Zhang, B. J. Li and F. Deng, *Catal. Commun.*, 2009, **10**, 920–924.
- 59 H. Chen, H. H. Ruan, X. L. Lu, J. Fu, T. Langrish and X. Y. Lu, *Mol. Catal.*, 2018, **445**, 94–101.
- 60 W. Li, G. L. Fan, L. Yang and F. Li, *ChemCatChem*, 2016, **8**, 2724–2733.
- 61 M. A. Aramendía, V. Borau, C. Jiménez, J. M. Marinas, J. R. Ruiz and F. J. Urbano, *Appl. Catal., A*, 2003, **244**, 207–215.
- 62 Q. Hu, L. Yang, G. L. Fan and F. Li, *ChemNanoMat*, 2016, **2**, 888–896.
- 63 From <http://webbook.nist.gov/>.
- 64 G. Allen and H. J. Bernstein, *Can. J. Chem.*, 1955, **33**, 1055–1061.
- 65 V. K. Díez, C. R. Apesteguía and J. I. D. Cosimo, *Catal. Today*, 2000, **63**, 53–62.
- 66 G. M. González Maldonado, R. S. Assary, J. Dumesic and L. A. Curtiss, *Energy Environ. Sci.*, 2012, **5**, 6981–6989.
- 67 R. González, R. Martínez and P. Ortiz, *Macromol. Chem. Phys.*, 1992, **193**, 1–9.
- 68 M. Boronat, A. Corma and M. Renz, *J. Phys. Chem. B*, 2006, **110**, 21168–21174.
- 69 V. A. Ivanov, J. Bachelier, F. Audry and J. C. Lavalley, *J. Mol. Catal.*, 1994, **91**, 45–59.
- 70 M. X. Su, W. Z. Li, T. W. Zhang, H. S. Xin, S. Li, W. Fan and L. L. Ma, *Catal. Sci. Technol.*, 2017, **7**, 3555–3561.